

Free-Breathing Liver Fat, R_2^* and B_0 Field Mapping Using Multi-Echo Radial FLASH and Regularized Model-based Reconstruction

Zhengguo Tan^{1,2}, Christina Unterberg-Buchwald³, Moritz Blumenthal¹, Nick Scholand¹, Philip Schaten¹, Christian Holme¹, Xiaoqing Wang^{1,2}, Dirk Raddatz⁴, and Martin Uecker^{1,5}

¹Institute for Diagnostic and Interventional Radiology, University Medical Center Göttingen, Göttingen, Germany

²Department of Artificial Intelligence in Biomedical Engineering, University of Erlangen–Nuremberg, Erlangen, Germany

³Department of Cardiology and Pulmonology, University Medical Center Göttingen, Göttingen, Germany

⁴Clinic of Gastroenterology, Gastrointestinal Oncology and Endocrinology, University Medical Center Göttingen, Göttingen, Germany

⁵Institute of Biomedical Imaging, Graz University of Technology, Graz, Austria

November 28, 2022

Abstract

This work introduced a stack-of-radial multi-echo asymmetric-echo MRI sequence for free-breathing liver volumetric acquisition. Regularized model-based reconstruction was implemented in Berkeley Advanced Reconstruction Toolbox (BART) to jointly estimate all physical parameter maps (water, fat, R_2^* , and B_0 field inhomogeneity maps) and coil sensitivity maps from self-gated k -space data. Specifically, locally low rank and temporal total variation regularization were employed directly on physical parameter maps. The proposed free-breathing radial technique was tested on a water/fat & iron phantom, a young volunteer, and obesity/diabetes/hepatic steatosis patients. Quantitative fat fraction and R_2^* accuracy were confirmed by comparing our technique with the reference breath-hold Cartesian scan. The multi-echo radial sampling sequence achieves fast k -space coverage and is robust to motion. Moreover, the proposed motion-resolved model-based reconstruction allows for free-breathing liver fat and R_2^* quantification in multiple motion states. Overall, our proposed technique offers a convenient tool for non-invasive liver assessment with no breath holding requirement.

1 Introduction

Quantitative parameter mapping of the liver is of interest in basic research and clinical practice. Specifically, quantitative proton density fat fraction (PDFF) and R_2^* maps have been shown to be non-invasive imaging biomarkers for hepatic steatosis [1, 2] and iron overload [3, 4], respectively. Originating from the two-echo chemical-shift-encoded Dixon method [5] for qualitative water/fat separation, quantitative assessment of liver fat and iron decomposition firstly requires multi-echo chemical-shift encoding (e.g. low flip angle multi-gradient-echo acquisition). Conventional acquisition methods require subjects to hold their breath. Therefore, incomplete breath hold or in compliant patients can induce pronounced image artifacts, thereby hampering the quantification of liver fat and R_2^* .

To address the respiratory motion problem, several recent works proposed free-breathing liver fat and R_2^* mapping. Armstrong et al. [6] and Zhong et al. [7, 8] proposed to use stack-of-radial multi-echo sampling with bipolar gradients. Sampled echoes were binned into four respiratory phases and reconstructed via non-uniform FFT (NUFFT) [9]. Liver fat and R_2^* maps are quantified via physics modeling [10–12] and image-space fitting [13–15]. Schneider et al. [16] employed model-based reconstruction [17–19] to jointly reconstruct water, fat, and R_2^* maps directly from k -space data with spatial and temporal total variation (TV) regularization, whereas the B_0 field inhomogeneity map was pre-calibrated [14] and was then kept fixed during iterative reconstruction. Wang et al. [20] implemented inversion recovery (IR) magnetization preparation before multi-echo readouts and applied the multi-tasking reconstruction technique [21] to reconstruct respiratory motion resolved multi-echo and IR images. Subsequently, these images were used for model fitting [14] to obtain quantitative fat, R_2^* , and water-specific T_1 maps. Starekova et al. [22] proposed a 2D acquisition scheme with a non-local means [23] motion-corrected averaging technique.

Among these free-breathing techniques, only the work from Schneider et al. employed model-based reconstruction. However, this work calibrated sensitivities and field map based on an a fast initial reconstruction with lower quality. This is suboptimal, as these maps are then either affected by inconsistencies due to lower temporal resolution when averaging data from multiple motion states or affected by undersampling artefacts. Joint estimation of the field map can reduce errors. It was proposed before using a smoothness prior on the B_0 field map via first- or second-order finite-difference regularization [24–26], Integration of the field map into a motion-resolved reconstruction for free-breathing liver imaging poses substantial additional challenges, as the B_0 field map appears as a non-linear term in the water/fat separation and may change rapidly at water-tissue interfaces.

The contribution of this work is two-fold: First, to achieve more efficient and faster acquisition, our work combined multi-echo asymmetric-echo radial fast low-angle shot (FLASH) with stack-of-stars volumetric acquisition [27] for free-breathing acquisition. Second, we implemented a regularized model-based

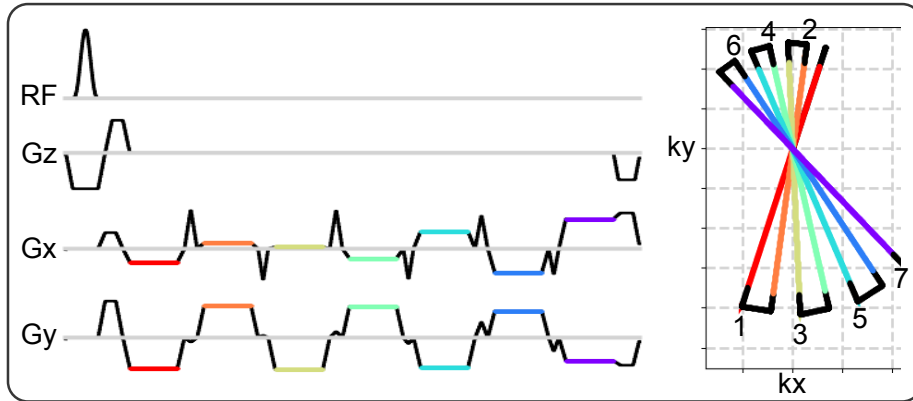


Figure 1: (Left) One representative repetition time (TR) block of the proposed multi-echo asymmetric-echo radial sequence. (Right) The corresponding k -space trajectory. The echoes are color coded, indicating the period when ADC is switched on, while the dark solid lines indicate either the ramp or the blip gradients.

reconstruction method for joint estimation of all quantitative parameter maps as well as B_0 map, and coil sensitivity maps directly from k -space data, thus extending the approach used by Schneider et al. We solved the nonlinear inverse problem via iteratively regularized Gauss-Newton method (IRGNM) [28] with the alternating direction method of multipliers (ADMM), allowing for generalized regularization terms [29]. We validated the proposed acquisition and reconstruction methods by comparing with the reference breath-hold Cartesian scan [15] in volunteers and patients diagnosed with obesity, diabetes, or non-alcoholic fatty liver disease (NAFLD).

2 Theory

2.1 Multi-Echo Radial Sampling

Data acquisition is based on the multi-echo radial sampling sequence [30]. As depicted in Fig. 1, seven gradient echoes per RF excitation were acquired. All radial spokes within one frame were uniformly distributed in k -space and the angle increment between frames was the small Golden angle [31] ($\approx 68.75^\circ$). The angles of the radial spokes within one frame are $\theta_{l,m} = 2\pi \cdot [(l-1) \cdot N_{\text{echo}} + m - 1] / (N_{\text{echo}} \cdot N_{\text{shot}})$ with l and m being the excitation and echo index, respectively. To shorten TE, TR as well as scan time, asymmetric echoes (i.e. partial Fourier readouts) [32] were employed in combination with multi-echo sampling.

2.2 Nonlinear Signal Model

Parallel MRI [33–35] simultaneously receives signals from multiple receiver coils, and is extendable to include multiple echoes when using long echo-train MRI sequences,

$$y_{j,m}(t) = \int d\vec{r} e^{-i2\pi\vec{k}(t)\cdot\vec{r}} c_j(\vec{r}) \rho_m(\vec{r}) , \quad (1)$$

with c_j and ρ_m being the j th coil sensitivity map and the m th echo image, respectively. $y_{j,m}(t)$ is the acquired multi-coil multi-echo k -space data. In the case of gradient echoes, ρ_m is governed by

$$\rho_m = \left(\sum_i I_i \cdot e^{i2\pi f_i \text{TE}_m} \cdot e^{-R_{2i}^* \text{TE}_m} \right) \cdot e^{i2\pi f_{B_0} \text{TE}_m} , \quad (2)$$

where the first term sums up signals from all chemical species (indexed by i), characterized by their corresponding proton density (I_i), resonance frequency (f_i) and relaxation rate (R_{2i}^*). Here, the dependency on the spatial coordinates \vec{r} is suppressed for simplicity. In addition, the echo signal is modulated by the B_0 field inhomogeneity. TE_m denotes the m th echo time.

This generalized multi-species signal can be simplified to only two compartments [10–12], i.e. water (W) and fat (F),

$$\rho_m = \left(\text{W} + \text{F} \cdot z_m \right) \cdot e^{-R_2^* \text{TE}_m} \cdot e^{i2\pi f_{B_0} \text{TE}_m} . \quad (3)$$

The chemical-shift phase modulation from fat is denoted as z_m with the 6-peak fat spectrum [11], while all fat peaks are assumed to have an equal R_2^* [36]. W and F are complex-valued, while R_2^* and f_{B_0} are real.

Given the above MR signal model, the nonlinear forward model in multi-coil multi-echo acquisition can be written in the operator form

$$y_{j,m} = F_{j,m}(x) := P_m \mathcal{F} M \mathcal{S} \mathcal{B} , \quad (4)$$

with $x = (\text{W}, \text{F}, R_2^*, f_{B_0}, \dots, c_j, \dots)^T$. $F_{j,m}(x)$ denotes the forward operator. j is the coil index ($j \in [1, N_{\text{coil}}]$), and m the echo index ($m \in [1, N_{\text{echo}}]$). The nonlinear operator (\mathcal{B}) calculates echo images according to the parameter maps in x and the corresponding signal model as given in Equation (3). Every echo image is then pointwisely multiplied by every coil sensitivity map in x , as denoted by the operator \mathcal{S} . Afterward, all multi-echo coil images are masked to be restricted to a given field of view (FOV) (M), Fourier-transformed (\mathcal{F}), and sampled (P) at each echo. In addition, because radial sampling acquires k -space data within a circular region, the k -space filter [37] is applied to the sampling pattern to suppress potential checker-board artifacts.

2.3 Model-based Nonlinear Inverse Reconstruction

The joint estimation of the unknown x is a nonlinear inverse problem,

$$\begin{aligned}
& \text{minimize} \quad \sum_t \sum_m \sum_j \|y_{j,m,t} - F_{j,m,t}(x)\|_2^2 \\
& \quad + \lambda_1 \|\mathcal{L}(E_1 x)\|_1 + \lambda_2 \|\text{TV}_t(E_2 x)\|_1 \\
& \quad + \lambda_3 [\|x\|_2^2 + \|T_{f_{B_0}} f_{B_0}\|_2^2 + \|T_C C\|_2^2] \\
& \text{subject to} \quad R_2^* \geq 0
\end{aligned} \tag{5}$$

The unknown x in this problem contains respiratory-motion-resolved model parameter maps (W , F , R_2^* , and f_{B_0}) as well as coil sensitivity maps, and thus has the shape of $[N, N, 4 + N_{\text{coil}}, N_{\text{bin}}]$. Here, $[N, N]$ corresponds to the image matrix size, 4 is the total number of model parameters, and N_{bin} is the number of respiratory bins.

The locally low rank (LLR) regularization \mathcal{L} with the regularization strength λ_1 was applied onto the parameters W , F and R_2^* . These parameter maps were extracted from the complex x matrix using the extraction operator E_1 . The block size of the LLR constraint was 16×16 with random shifts of the blocks among iterations.

Temporal TV regularization [38] with the regularization strength λ_2 was applied onto all model parameter maps (W , F , R_2^* , and f_{B_0}), which can be extracted via the operator E_2 .

In addition, ℓ^2 regularization with the regularization strength λ_3 was applied to all unknowns. To enforce spatial smoothness of the B_0 and coil sensitivity maps, the Sobolev-norm weighting [28] was utilized to penalize high spatial frequencies,

$$T = \mathcal{F}^{-1} \left(1 + w \cdot \|\vec{k}\| \right)^{-h} \mathcal{F} \tag{6}$$

h is set as 16 for both maps, while $w_{f_{B_0}} = 22$ and $w_C = 220$ for the f_{B_0} and coil sensitivity maps, respectively. \vec{k} is a 2D Cartesian grid ranging from -0.5 to 0.5 [30].

The objective functional in Equation (5) was solved by IRGNM with ADMM. For details about this algorithm please refer to Appendices A and B. Our implementation enables flexible selections of regularization terms.

We compared our proposed regularization strategy against only ℓ^2 regularization (i.e. removal of the ℓ^1 terms in Equation (5)) as well as the temporal TV regularization method without B_0 update (similar to the work from Schneider et al. [16]). Keeping B_0 constant during model-based reconstruction can be realized via setting the forward model's adjoint of derivative term with respect to B_0 as 0 (Previously, this has been applied to nonlinear inversion as parallel imaging to keep coil sensitivity maps constant during iterative reconstruction [28]).

Table 1: Measured volume of iron, water and peanut oil solutions for the eight tubes

Solution (mL)	Tube 1	Tube 2	Tube 3	Tube 4	Tube 5	Tube 6	Tube 7	Tube 8
Iron	0.5	1.0	2.0	0	0.5	1.0	0	0
Water	50	50	50	45	45	45	40	0
Fat	0	0	0	5	5	5	10	50

3 Methods

3.1 Phantom Experiments

A water/fat & iron phantom [39, 40] was constructed. Details of this phantom are provided in Fig. 2 and Table 1. Due to water lost as steam in the preparation of the water and fat emulsion, the actual fat fraction was higher than prescribed in Table 1. Therefore, the actual fat fraction values of every tube were validated using the standard Siemens MR spectroscopy (MRS) protocol. MRI experiments were conducted with an 18-channel body matrix coil together with a spine coil on 3 T (Skyra, Siemens Healthineers, Erlangen, Germany). The proposed multi-echo radial sampling sequence was used with the following parameters: FOV 200 mm, base resolution 160, spatial resolution $1.25 \text{ mm} \times 1.25 \text{ mm} \times 3.5 \text{ mm}$, bandwidth 1040 Hz/pixel, flip angle 4° , asymmetric echo [32] of 30 %, TE 1.07, 2.35, 3.23, 4.51, 5.39, 6.67, 7.55 ms and TR 8.81 ms.

3.2 In Vivo Experiments

For in vivo scans, the same coils and MRI system were used. Two radial protocols were implemented, one with a smaller field of view (FOV) 320 mm for subjects with relatively small body size (Volunteer #1), and another with a larger FOV 410 mm which fits well for obese patients (Patient #1 to #9). Breath-hold multi-echo Cartesian Dixon MRI was used as the reference. Detailed parameters are provided in Table 2. Although the Cartesian scan requires one single breath hold and is fast, it captures only one motion state. In contrast, the proposed radial scan allows for free breathing, but requires longer scan time (2:47 min). We therefore, also investigated the effectiveness of the proposed motion-resolved model-based reconstruction on retrospectively undersampled (shortend) radial data corresponding to a scan time of 1:24 min.

One volunteer and twenty obesity/diabetes/NAFLD patients were scanned with both the multi-echo radial sampling sequence and the Cartesian DIXON sequence. The data for five patients were excluded because the automatic calibration of the resonance frequency used was the fat instead of the water peak, which then causes the reconstruction to fail. While this can be corrected in post-processing, this is not yet implemented. All subjects gave written informed

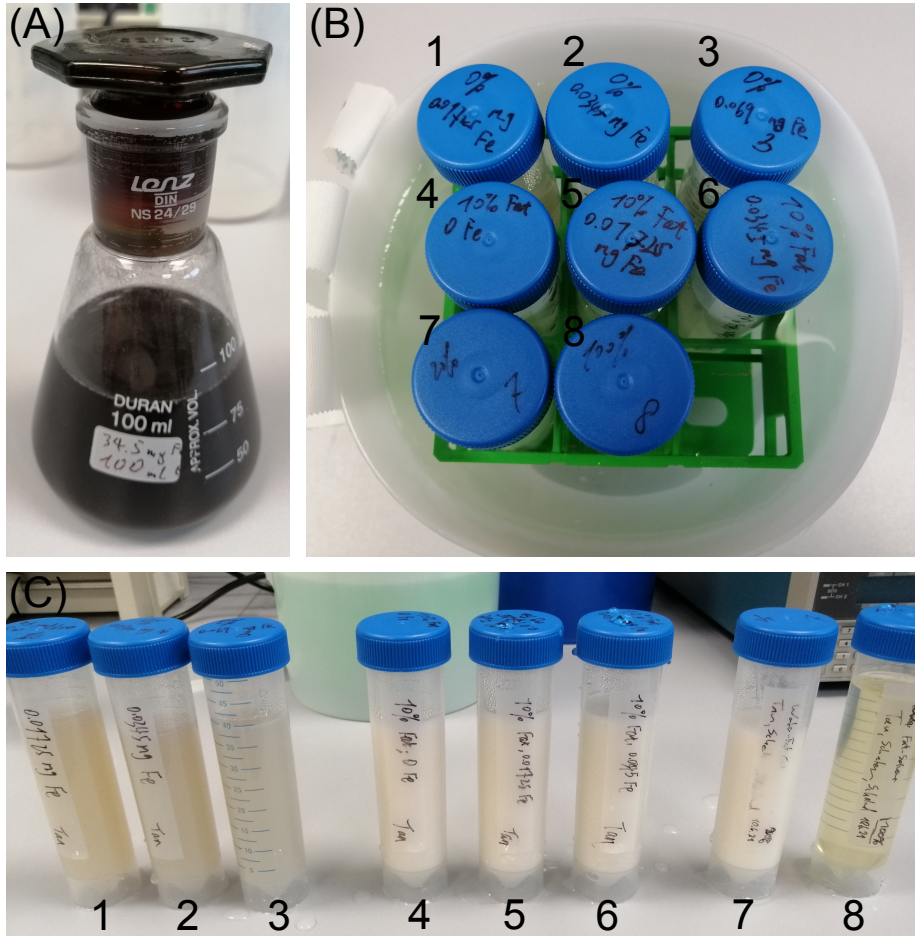


Figure 2: Photos of the constructed water/fat & iron phantom. (A) 34.5 mg iron nano particle diluted in 100 mL distilled water. (B) Phantom layout with eight tubes as listed in (C).

Table 2: Imaging parameters for (left) the breath-hold Cartesian reference and (right) the proposed free-breathing multi-echo radial acquisition with two different FOV

	Cartesian	Radial	Radial
Flip angle ($^{\circ}$)	4	4	4
Bandwidth (Hz/pixel)	1080	1090	1090
Asymmetric echo	None	30 %	30 %
Number of echoes	6 ^a	7 ^b	7 ^c
Repetition Time (ms)	9	8.35	8.39
FOV (mm \times mm)	410 \times 348	320 \times 320	410 \times 410
Pixel size (mm \times mm)	2.56 \times 2.56	1.6 \times 1.6	1.6 \times 1.6
Base resolution	160	200	256
Slice thickness (mm)	3.5	3.5	3.5
Slice resolution (%)	50	100	100
Slice oversampling (%)	25	25	25
Number of slices	64	48	48
Scan time (min:sec)	0:20	2:45	2:47

^a Echo times are 1.06, 2.46, 3.69, 4.92, 6.15, 7.38 ms;

^b Echo times are 0.98, 2.20, 3.04, 4.26, 5.10, 6.32, 7.16 ms;

^c Echo times are 0.98, 2.21, 3.05, 4.28, 5.12, 6.35, 7.19 ms.

consent before MRI in compliance with the regulations established by the local ethics committee. A summary of all subjects is given in Table 3, including the age, gender, height, weight, and the body mass index (BMI).

3.3 Model-based Reconstruction

In the spirit of reproducible and open research, the proposed regularized model-based reconstruction is made publicly available in BART [41]. Scripts to produce the experiments are available at <https://github.com/mrirecon/multi-echo-liver> upon publication. A brief description of the reconstruction procedure is given here.

Pre-Processing

The acquired multi-coil multi-echo data was compressed to ten virtual coils via principal component analysis [42]. The multi-echo sampling trajectory was corrected for gradient delays using the radial spoke intersections for gradient delay estimation (RING) method [43]. RING determines the intersection points of different radial spokes. Afterward, RING estimates the gradient delay coefficients given the position of the intersection points. RING was applied to every echo to estimate its corresponding gradient delay coefficients, which were then used to correct the trajectories.

Table 3: Summary of Subjects Participated in the Study

	Age	Gender	Height (cm)	Weight (kg)	BMI (kg/m ²)
Volunteer #1	27	F	155	60	25.0
Patient #1	55	M	184	105	31.0
Patient #2	60	F	172	105	35.5
Patient #3	64	F	164	80	29.7
Patient #4	60	F	153	112	47.8
Patient #5	44	F	165	94	34.5
Patient #6	43	F	165	165	60.6
Patient #7	65	M	176	98	31.6
Patient #8	55	F	156	88	36.2
Patient #9	54	F	160	68	26.6
Patient #10	62	M	202	100	24.5
Patient #11	67	M	176	99	32.0
Patient #12	26	F	178	180	56.8
Patient #13	69	M	191	134	36.7
Patient #14	61	M	173	114	38.1
Patient #15	51	M	169	101	35.4

Binning

In this work, the singular spectrum analysis (SSA-FARY) technique [44] was adapted for self-gating of respiratory motions. SSA-FARY combines the ideas of time-delayed embedding and principal component analysis, and allows for robust extraction of oscillatory motion signals such as respiration from an auto-calibration (AC) region. In particular, for a periodic signal contained in the AC region, SSA-FARY yields a quadrature pair, which can be used for self-gating. Such a quadrature pair can be thought of as a generalized sine-cosine-pair describing the respective periodic motion and can be represented by a phase-portrait, where an angle of 0° states the beginning and 360° states the end of a motion cycle.

In this work, we chose to split the respiratory motion into $N = 4$ bins, hence, each bin represents a circular sector with a central angle of $360^\circ/N$. Then, the respiratory motion state at a given time is determined by the respective angle defined by the quadrature pair. As one echo train was relatively short, only the first echo was extracted for SSA-FARY.

Note that although more respiratory bins can improve the temporal resolution, it leads to fewer radial spokes per bin. Such a trade-off can be alleviated via the temporal TV regularization. However, we observed that increasing bins did not significantly affect the reconstructed image quality (results not shown). Since the reference Cartesian scan was performed during end expiration, we used the end-expiration bin of the radial scan for comparison.

Initialization

Off-resonance phase modulation causes phase wrapping along the echoes, especially in the case of large B_0 field inhomogeneity. Consequently, multiple local minima could occur for the field map f_{B_0} . To prevent this, the f_{B_0} map was initialized from a model-based three-point water/fat separation [30]. W and F were initialized as 0.1. R_2^* and coil sensitivity maps were initialized as 0.

Iterative Reconstruction

For the model-based reconstruction, the regularization strength in Equation (5) (e.g. λ_1 , λ_2 , and λ_3) is reduced along Newton steps, e.g. $\lambda_i^{(n)} = \lambda_i/D^{n-1}$ for λ_1 , with n being the n th Newton iteration and the reduction factor $D > 1$. $D = 3$ was used in this work. For ADMM, the maximum number of iterations in each Newton step were given as: $n_{\text{maxiter}} = \min(M, 10 \times 2^{-\ln \lambda^{(n)}})$, where M was set as 200. Consequently, the maximal iterations gradually increase along the Newton steps.

In this work, eight Newton steps were employed, and the ADMM penalty parameter ρ was set as 0.001. For the regularization terms in Equation (5), we set $\lambda_1 = 0.0003$, $\lambda_2 = 0.1$, and $\lambda_3 = 1$. The scaling of the F, R_2^* , and B_0 maps was set as 1.6, 0.001, and 1, respectively. All reconstructions were performed on a Tesla V100-SXM2 32 GB GPU (NVIDIA, Santa Clara, CA, USA).

Post-Processing

With the reconstructed water and fat images, fat fraction (FF) maps can be computed taking into account the magnitude discrimination [45], i.e. $\text{FF} = 1 - |W|/(|W| + |F|)$ for pixels in which water dominates.

4 Results

With the proposed multi-echo radial FLASH acquisition and model-based reconstruction, Fig. 3 shows the results of the in-house built water/fat & iron phantom. The FF values of every tube are validated against the MRS measurements. The FF values of all tubes match well between the two measurements, as shown in Fig. 4.

Fig. 5 shows the reconstructed FF and R_2^* maps of Patients #1 and #2 from the reference breath-hold Cartesian and the proposed free-breathing radial scan, respectively. The R_2^* maps from Cartesian scans suffer from noise in the middle region (likely due to undersampling in the phase-encoding direction). Moreover, as pointed out by the yellow arrows, incomplete breath hold results in artifacts in the R_2^* maps. For model-based reconstruction of the parameter maps (W, F, R_2^* and f_{B_0}) from the radial scan, three different versions were compared: ℓ^2 , temporal TV without B_0 update (as employed by Schneider et al. [16]), LLR plus temporal TV with B_0 update. The results show that residual streaking artifacts can be suppressed via the use of spatial LLR and temporal

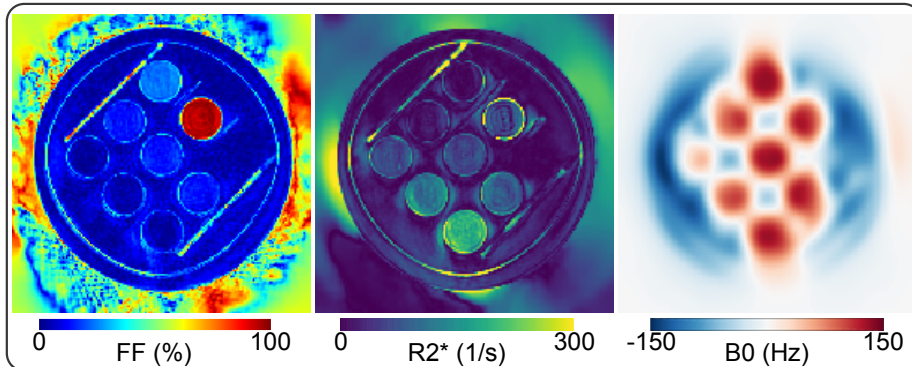


Figure 3: Multi-echo radial FLASH acquisition and model-based reconstruction results of the water/fat & iron phantom built in-house. Displayed images are FF, R_2^* , and B_0 maps, respectively.

TV regularization. An update of the B_0 map during the model-based iterative reconstruction improves the reconstructed FF and R_2^* maps. The current initialization strategy used only the first three echoes with limited coverage of k -space, which supplies only a rough estimate of the B_0 map. Performing B_0 updates can help to recover a more accurate B_0 map by using information from all seven echoes as shown in Fig. 6. All subsequent figures use the same color maps for FF and R_2^* as in Fig. 5.

Further, to demonstrate the effectiveness of using SSA-FARY for the motion resolved free-breathing radial scan, Fig. 7 compares the reference breath-hold Cartesian scan and the proposed free-breathing radial scan for Patient #1 in the reformatted coronal view. While the liver dome region shows hyper R_2^* intensity from the Cartesian scan, consistent R_2^* values are visible from the proposed radial scan and model-based reconstruction. Such hyper intensity may be caused by the fast B_0 field change in the liver dome region, which is close to the lung with much lower MR signal. On the other hand, respiratory motion is well separated across the four frames. As shown in the self-gating AC signal plot in Fig. 7 (B), A total of 330 radial spokes were acquired during the free-breathing scan. When plotted into the phase portrait, the pair of empirical orthogonal functions (EOF) can be equally divided into four angular blocks, representing four distinct respiratory motion states.

Fig. 8 depicts the Bland-Altman as well as scatter plots comparing the reference breath-hold Cartesian scan and the proposed free-breathing radial scan. For this quantitative analysis, three regions of interest (ROI) were selected for every subject and the mean value of every ROI was used for plotting. In the Bland-Altman plots, the x and y axis represents the mean and difference values between these two scans, respectively. The central dotted line along the x-axis shows the mean bias between these two scans and is computed by averaging the difference values. The upper and lower dotted lines show the limits of agreement

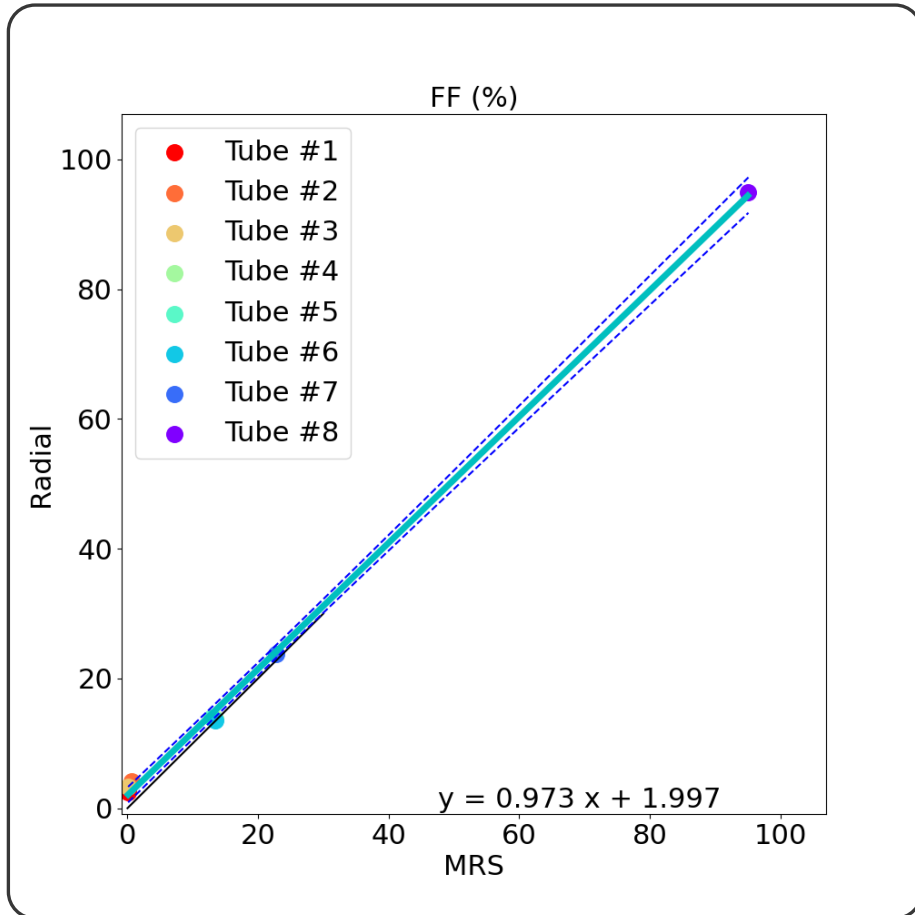


Figure 4: Quantitative analysis of FF values for the eight tubes via linear regression between the standard MR Spectroscopy (MRS) and the proposed multi-echo radial acquisition with model-based reconstruction.

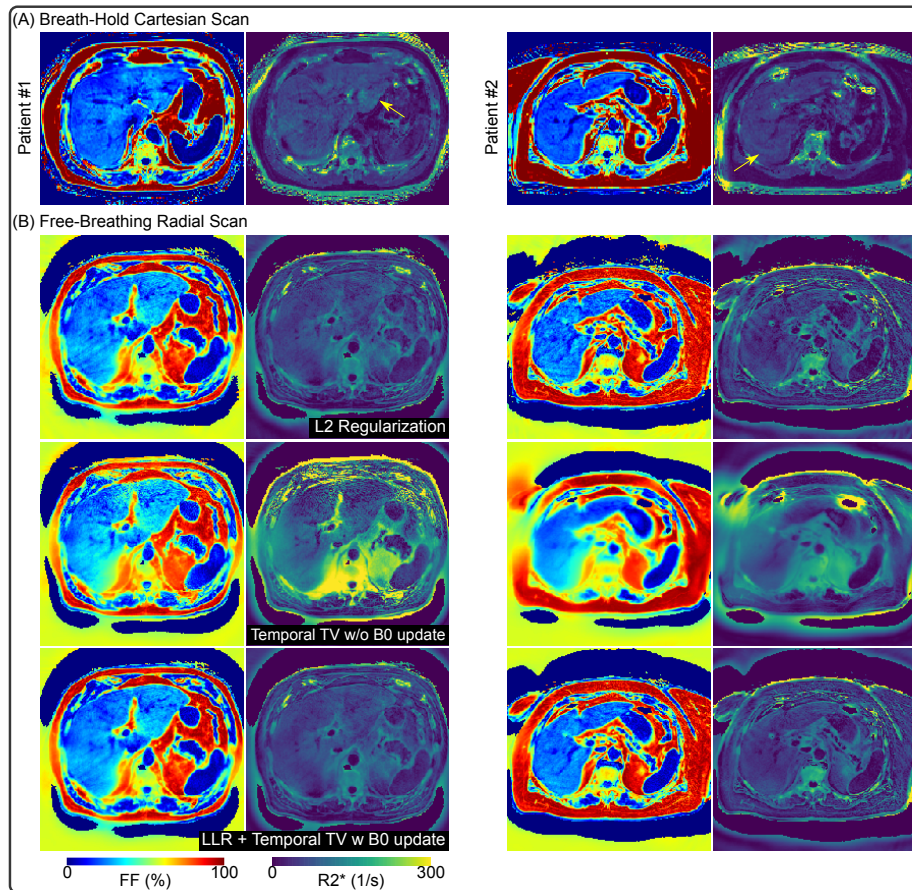


Figure 5: Comparison of (A) the reference breath-hold Cartesian scan and (B) the proposed free-breathing radial scan on Patients #1 and #2. Furthermore, for the radial data in (B), we compared three different regularizations: L2 regularization, temporal TV regularization without B_0 update, and the proposed spatial LLR and temporal TV regularization with B_0 update.

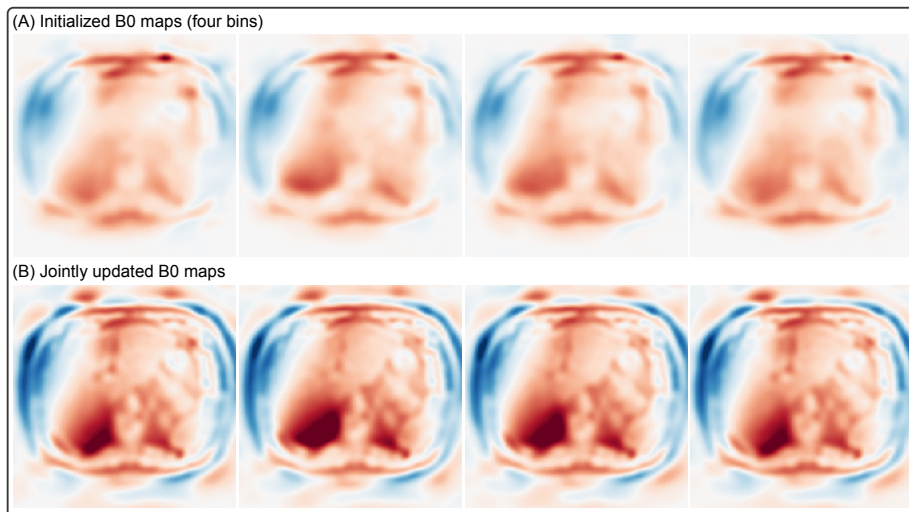


Figure 6: (A) Initial B_0 maps of four respiratory bins for the model-based reconstruction without B_0 update in Fig. 5. (B) Jointly updated B_0 maps of four respiratory bins. Joint update using seven echoes helps to recover more details in the B_0 maps.

(mean bias $\pm 1.96 \times$ standard deviation of difference). In the scatter plots, the x and y axis represents the mean values of the Cartesian and the radial scan, respectively. In addition, linear regression was performed. The slope of the fitted curve for both FF and R_2^* values is close to 1, indicating a good match between the Cartesian and the radial measurements.

Tables 4 and 5 further summarize both the mean and the standard deviation values of every ROI and every patient. Overall, the patients in this work cover wide ranges of FF and R_2^* values, and hence are representative for the validation of the proposed method. Moreover, the quantitative analysis results reveal two important clinical indications.

First, obese patients may not necessarily have fatty liver disease. Patient #6 is diagnosed with obesity, and shows the highest BMI in Table 3. For this patient, however, ultrasound is not able to penetrate through the thick subcutaneous fat layer to assess the liver fat content. As shown in Fig. 9, both breath-hold Cartesian and free-breathing radial scans are able to provide quantitative FF and R_2^* maps. The liver regions exhibit relatively low FF values. This patient shows the lowest FF and R_2^* values among all subjects in this study (see Fig. 8). On the other hand, the R_2^* maps in both the transversal and sagittal views again suffer from hyper intensities in the Cartesian scan (as pointed by yellow arrows), while our proposed radial scan shows more homogeneous R_2^* maps.

Second, in our study, patients with hepatic steatosis may not necessarily be obese. Fig. 10 displays one volunteer and one patient with elevated FF

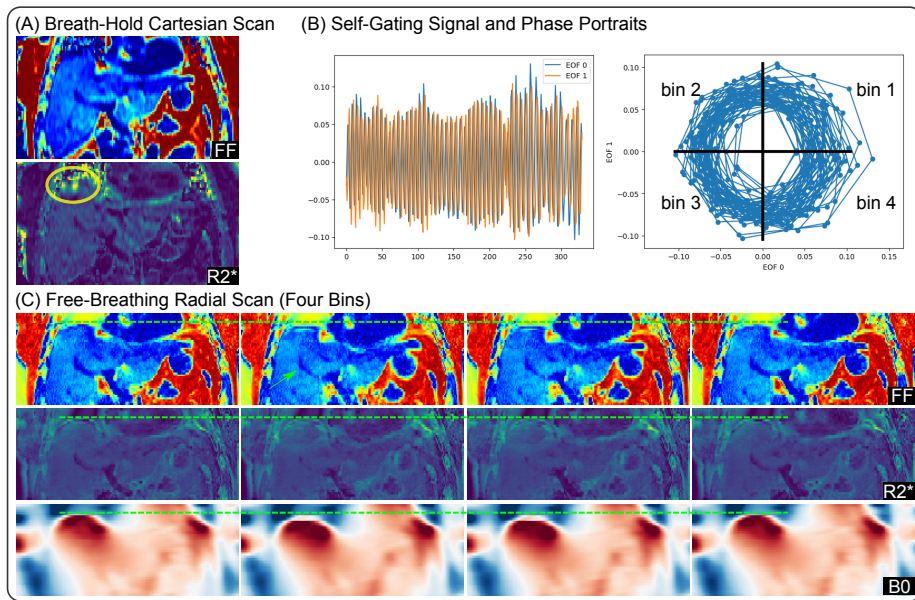
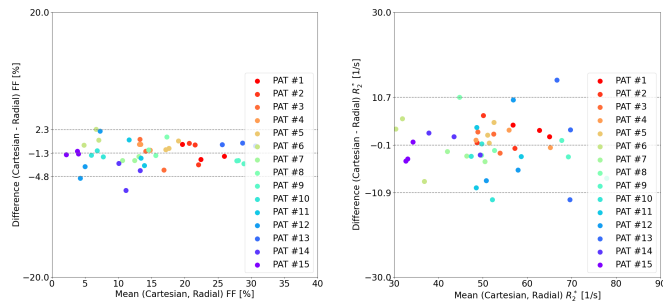


Figure 7: (A) One coronal-view FF and R_2^* map from breath-hold Cartesian scan of Patient #1. (B) Plots of self-gating signal and phase portraits. (C) Four coronal-view FF and R_2^* maps from free-breathing radial scan with self-gated motion-resolved model-based reconstruction. The R_2^* map in (A) suffers from hyper intensities in the liver dome region (yellow ellipse), whereas the proposed radial scan shows consistent R_2^* values.

(A) Bland-Altman plots comparing breath-hold Cartesian and free-breathing radial scans



(B) Linear regression between breath-hold Cartesian and free-breathing radial scans

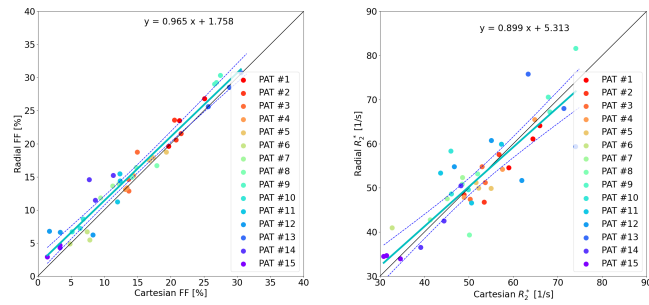


Figure 8: Quantitative analysis of reconstructed FF and R_2^* maps for all subjects comparing the reference breath-hold Cartesian scan and the proposed free-breathing radial scan, respectively.

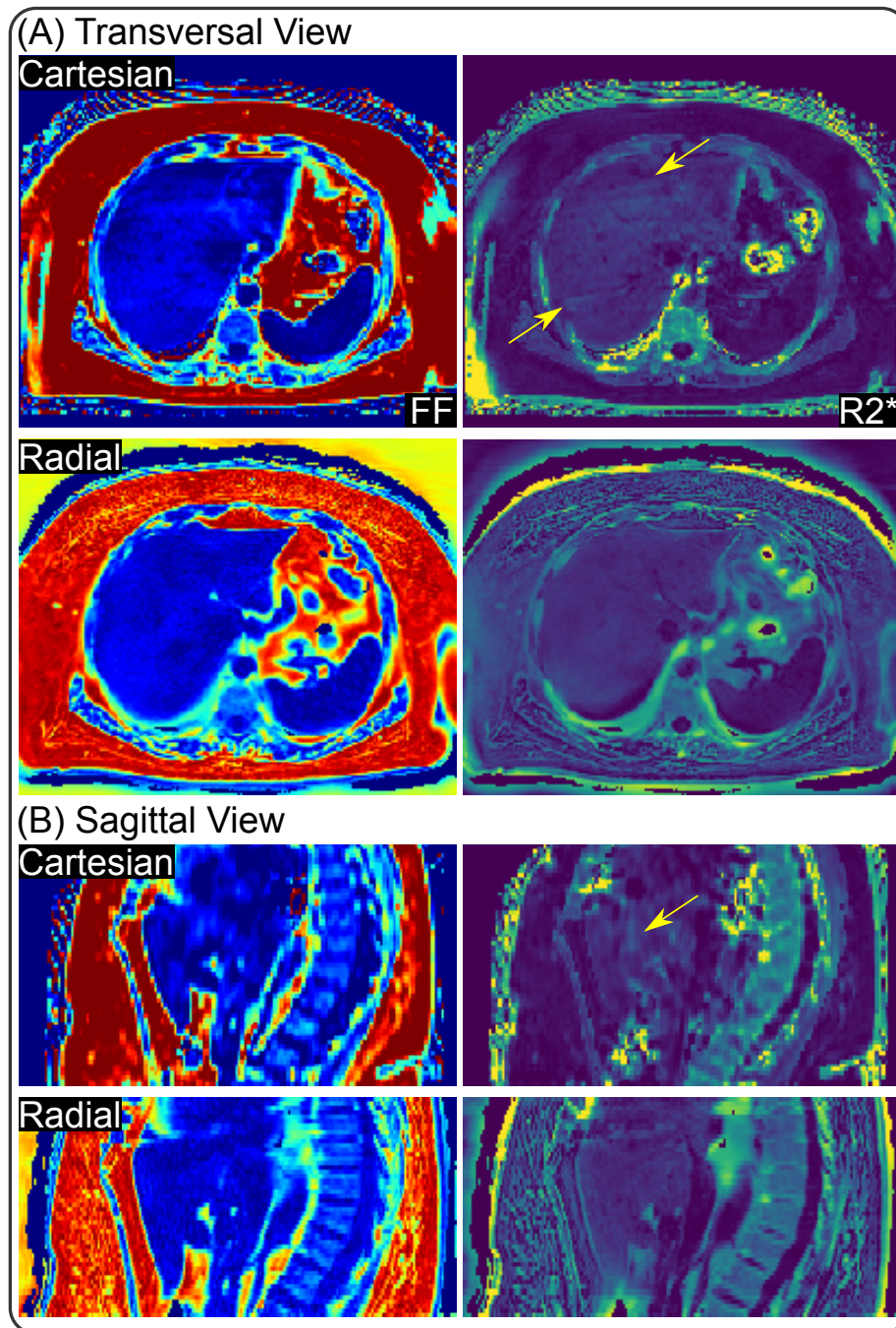


Figure 9: (A) Transversal view and (B) sagittal view of reconstructed FF and R_2^* maps in Patient #6 comparing the reference breath-hold Cartesian scan and the proposed radial scan, respectively. This patient shows definite obesity symptom (see Table 3), but has no fatty liver. In fact, the FF values of this patient is the lowest among all subjects (see also Fig. 8). Similar to the results of Patient #1 in Fig. 5, the Cartesian scan suffers from fold-in artifacts in the R_2^* maps (yellow arrows), while the proposed radial scan shows consistent R_2^* values.

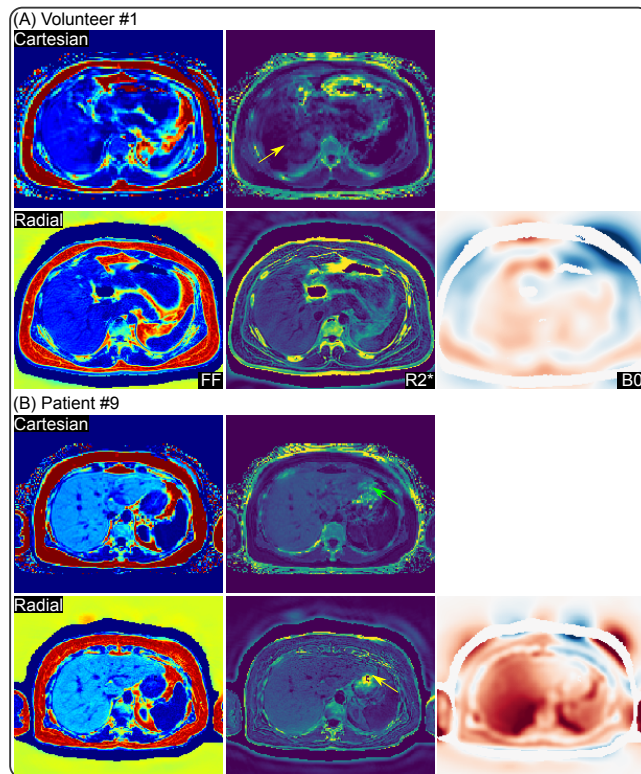


Figure 10: (A) Volunteer #1 and (B) Patient #9 with elevated FF values, but no clear symptom of obesity. In particular, Patient #9 was diagnosed with hepatic steatosis by the standard liver biopsy and ultrasound.

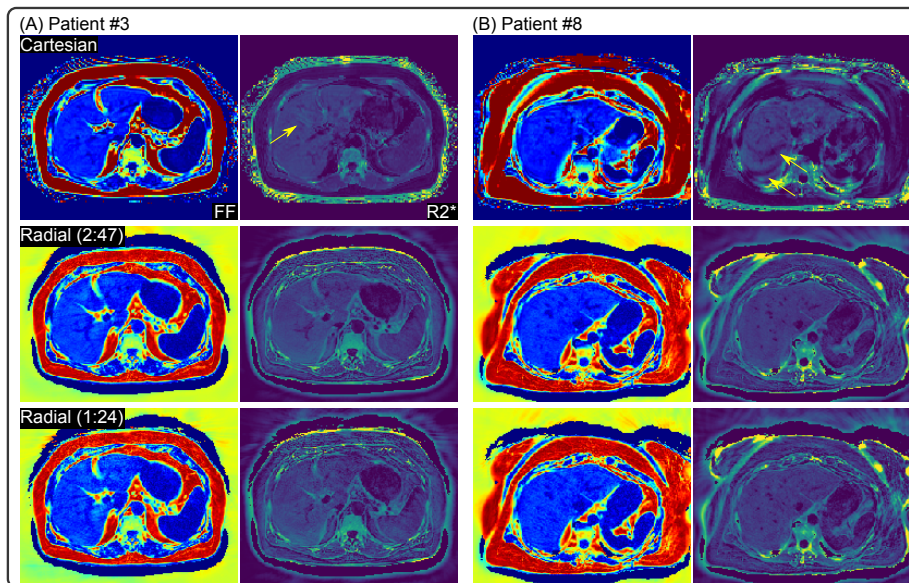


Figure 11: Comparison of FF and R_2^* maps for Patients (A) #3 and (B) #8 among the reference Cartesian scan, the free-breathing radial 2:47 min scan, and the free-breathing radial scan with retrospective two-fold undersampling, corresponding to a scan time of 1:24 min. Note the ripple-like artifact in the R_2^* map from the Cartesian scans due to incomplete breath hold (yellow arrows in the 1st row).

values from both the reference breath-hold Cartesian and the free-breathing radial scans. Patient #9 has hepatic steatosis as confirmed via liver biopsy and ultrasound diagnosis. However, neither of them shows the problem of obesity (see Table 3). Through Fig. 8 and Fig. 10, we also observe that hepatic steatosis is more likely to occur in elderly patients. Although fatty liver is also captured in the scan of Volunteer #1, this is rather a rare case among all young volunteers (results not shown here). On the other hand, in the left corner of the liver in Patient #9 (see the green arrows), R_2^* values from the Cartesian scan again are higher, possibly due to the fast B_0 change in this air-tissue interface, created by the empty region within the stomach.

Noteworthy, the reference Cartesian scan requires subjects to hold their breath. When subjects fail to perform breath holding, it may lead to image artifacts in the reconstruction. Figs. 10 and 11 (see yellow arrows) are such examples. Residual respiratory motion during the scan causes fast B_0 field drift [30] as well as signal variation. This situation makes the fitting of B_0 and R_2^* difficult. In this example, it results in the blurring artifact for Patient #3 and ripple-like artifact for Patient #8 (see yellow arrows) and unreliable R_2^* values. However, the proposed free-breathing radial scan is free of such artifacts.

Furthermore, we investigated reducing the acquired radial data by one-half,

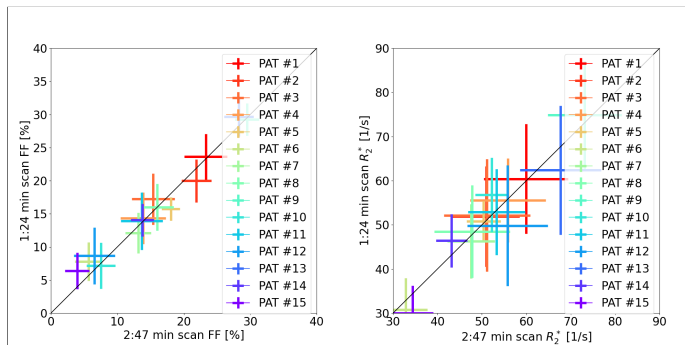


Figure 12: Quantitative analysis of the reconstructed FF and R_2^* maps from radial scans: actual acquisition (2:47 min) and retrospectively undersampled acquisition (1:24 min), respectively.

to explore the feasibility of the proposed motion-resolved model-based reconstruction on retrospectively undersampled data. As shown in Figs. 11 and 12 as well as in the right column of Tables 4 and 5, retrospective undersampling increases standard deviation in the reconstructed FF and R_2^* maps, but the mean values agree well with the reconstruction on the 2:47 min scan (the center column).

This work uses joint estimation of all parameter maps by solving a nonlinear inverse problem. This includes simultaneous estimation of the coil sensitivity maps. Fig. 13 displays the ten coil sensitivity maps of the first respiratory bin in comparison to sensitivities estimated with ESPIRiT [46]. Since coil sensitivity maps from ESPIRiT are inherently normalized, normalization is also applied to the coil sensitivity maps from the model based reconstruction. The coil sensitivity maps from both methods are very similar inside the region with signal.

5 Discussion

This work introduced a stack-of-radial multi-echo radial FLASH sequence with partial Fourier readouts (i.e. asymmetric echo) for volumetric free-breathing liver acquisition. Moreover, this work introduced a regularized model-based reconstruction in BART to jointly estimate liver water, fat, R_2^* , B_0 field inhomogeneity maps, and coil sensitivity maps directly from acquired k -space data. This nonlinear inverse problem was solved by IRGNM with ADMM, allowing for generalized regularization terms in nonlinear reconstruction. To validate the proposed MRI sequence and reconstruction, a pilot study was conducted comprising young volunteers and patients diagnosed with obesity, diabetes, or hepatic steatosis. The reconstructed FF and R_2^* maps were further compared with the reference breath-hold Cartesian scan. We found good agreement be-

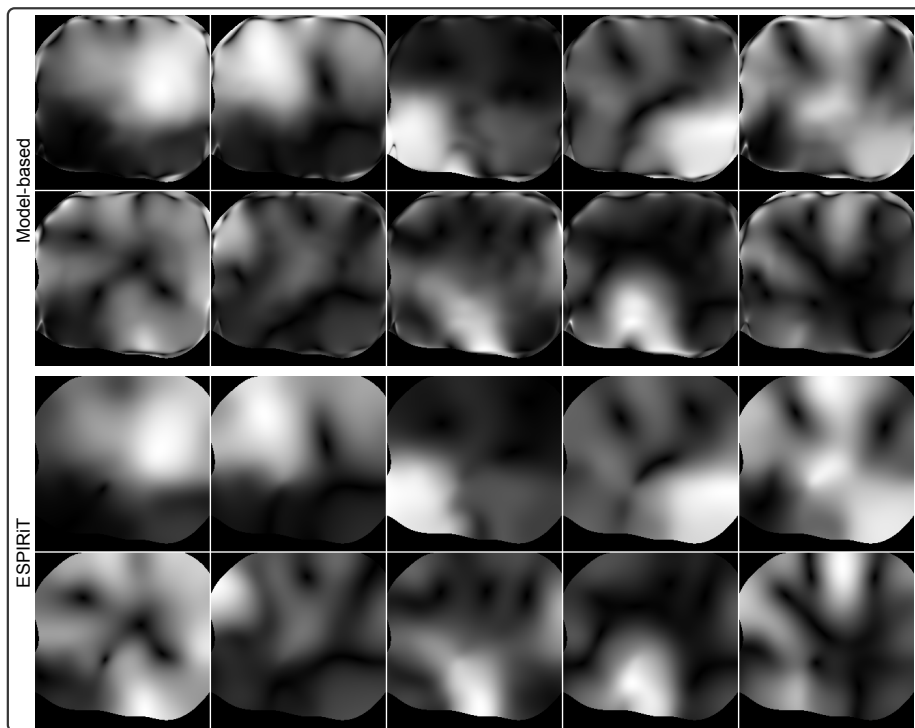


Figure 13: Magnitude of coil sensitivity maps for Patient #1 from (top) the proposed model-based method and (bottom) the ESPIRiT method.

tween the proposed free-breathing radial scan and the breath-hold Cartesian scan.

The R_2^* maps of Patient #1 from the proposed method are visually more blurred compared to the reference Cartesian scan, while the volunteer R_2^* map shows a sharp delineation of the liver and vessel borders. This may be due to the use of a larger FOV in the acquisition protocol for patients, which corresponds to higher undersampling. On the other hand, the larger body size of this patient may result in poorer receiver signals in the middle.

In model-based reconstructions, parameter maps are directly reconstructed from acquired k -space data. Therefore, regularizations can be directly imposed on parameter maps. An alternative approach is to reconstruct all echo images and then perform image-space parameter fitting [6–8, 20, 22]. In this case, advanced regularizations (e.g. ℓ^1 -Wavelet and low rankness) can be employed along the echo dimension. However, this study mainly focused on the comparison with the reference breath-hold Cartesian scan. In addition, this study also compared against another model-based reconstruction approach using temporal total variation regularization on water, fat and R_2^* maps, whereas B_0 and coil sensitivity maps were calibrated and kept constant [16].

This work initialized the B_0 field inhomogeneity map for every respiratory bin by the B_0 estimate from a 3-echo model-based reconstruction. As only three echoes were used for the reconstruction, this initialization procedure is relatively fast. Such B_0 initialization assures the convergence of large-scale model-based reconstructions on seven echoes and four respiratory bins. Recently, Zhang et al. proposed the solution interval method for nonlinear inverse problems [47]. However, abundant computation power is required to run the nonlinear least square fitting multiple times for the construction of solution intervals for every unknown. In general, nonlinear inverse problems consisting of non-convex phase variation is not trivial to be solved. Similar problems exist in multi-shot diffusion MRI as well. Recently, Hu et al. [48] proposed to jointly estimate diffusion-weighted magnitude and phase images to resolve the shot-to-shot phase variation. Similar to our work, this approach solves a non-linear non-convex inverse problem, but still requires good phase initialization.

There are several aspects of this study that can be further improved. No patient participated in this study showed symptoms of iron overload (i.e. elevated R_2^* values). To the best of our knowledge, iron overload is more likely to be seen in patients who require regular blood transfusions. These patients, however, are rather rare in obesity/diabetes clinics. Although lacking such patients, we showed the capability of our technique in quantifying iron overload in the phantom, as seen in Fig. 3, where Tube 3 results in the highest R_2^* value due to iron.

Joint estimation of all physical parameter maps and coil sensitivity maps is a nonlinear nonconvex inverse problem. Especially when including the B_0 field inhomogeneity map as one unknown, the reconstruction is sensitive to the initial guess and scaling of unknowns. Our implementation initialized the B_0 map with the previously proposed three-echo reconstruction [30], which indeed fostered convergence. Second, scaling of the fat, R_2^* , and B_0 maps was empirically

determined. Therefore, more intelligent B_0 estimation and automatic scaling of unknowns [49] would be logical directions.

Compared with the reference breath-hold Cartesian scan, our proposed radial sampling did not explore k_z unaligned undersampling strategies [50], which can further accelerate data acquisition.

While this work focused on liver fat and R_2^* mapping, the presented multi-echo radial sequence in principle is also applicable to brain imaging, which, would become rather interesting in combination with the above-mentioned k_z undersampling. Alternatively, one can also explore the possibility of multiple parametric mapping via extending the basic multi-echo radial acquisition to variable flip angles or magnetization preparation.

This work employed the recently proposed SSA-FARY technique for self-gating, where the determination of spokes as respiratory bins was based on polar angles in the phase portrait plot. This procedure did not take into account the radius of every spoke in phase portrait, which might cause problems in the case of irregular breathing. Therefore, it might make the self-gating technique more general considering the radius. Alternatively, it would be interesting to use pilot tone [51] for prospective respiratory binning during data acquisition.

The total reconstruction time for the whole liver took about 4 h on the Tesla V100 GPU. For clinical translation, further acceleration could be achieved via for example multiple GPU parallelization. This includes two aspects. First, the proposed reconstruction algorithm can be parallelized with multiple GPUs to accelerate the iterative minimization procedure. Second, currently slices are reconstructed in a sequential manner. This can be modified to distribute the slice reconstruction in parallel to further speed up the whole process. These aspects, however, are outside the scope of this work, which mainly focused on the technical development of the free-breathing model-based reconstruction method.

6 Conclusion

This work introduced a free-breathing liver fat and R_2^* quantification technique, comprising stack-of-radial multi-echo asymmetric-echo volumetric continuous acquisition and regularized non-linear model-based reconstruction. The generic model-based reconstruction framework in BART allows the flexible use of generalized regularization terms and is integrable with different physical models. This work uses this framework for joint estimation of time-resolved physical parameter maps (water, fat, R_2^* , and B_0) and coil sensitivity maps. The proposed method is validated against a reference breath-hold Cartesian scan on healthy volunteers and patients. This technique offers a non-invasive tool for quantitative liver assessment during free breathing.

A

To minimize the cost function in Equation (5), IRGNM linearizes the nonlinear forward model via Taylor expansion in each Newton step, thus the data-consistency term in Equation (5) becomes

$$\|DF(x_n)dx - [y - F(x_n)]\|_2^2 \quad (\text{A.1})$$

where the Jacobian $DF(x_n)$ denotes the derivative of the forward operator concerning the n th-step estimate. Given the initial guess as x_0 [28], one can denote $x = x_{n+1} - x_0 = x_n + dx - x_0$. As a result, Equation (A.1) becomes

$$\begin{aligned} & \|DF(x_n)(x + x_0 - x_n) - [y - F(x_n)]\|_2^2 \\ \Rightarrow & \|DF(x_n)x - [DF(x_n)(x_n - x_0) + y - F(x_n)]\|_2^2 \end{aligned} \quad (\text{A.2})$$

whose minimum occurs when its derivative is set to 0, and we obtain such a linear system equation,

$$Ax = b \quad (\text{A.3})$$

for which we denote $A := DF^H(x_n)DF(x_n)$ and $b := DF^H(x_n)\{DF(x_n)(x_n - x_0) + y - F(x_n)\}$.

With generalized ℓ_1 regularization, Equation (A.3) can be written in the ADMM form,

$$\begin{aligned} & \text{minimize } \|Ax - b\|_2^2 + \alpha \|z\|_1 \\ & \text{subject to } Tx - z = 0 \end{aligned} \quad (\text{A.4})$$

The updates can be derived,

$$\begin{cases} x^{(k+1)} := (A^H A + \rho T^H T / 2)[A^H b + \rho T^H (z^{(k)} - \mu^{(k)}) / 2] \\ z^{(k+1)} := \mathcal{T}_{\alpha/\rho}(Tx^{(k+1)} + \mu^{(k)}) \\ u^{(k+1)} := u^{(k)} + Tx^{(k+1)} - z^{(k+1)} \end{cases} \quad (\text{A.5})$$

The x update is solved by the conjugate gradient method, and the z update is computed via soft thresholding ($\mathcal{T}_{\alpha/\rho}$), where α is passed from IRGNM and iteratively reduced along Newton steps, $\alpha = 1/D^{n-1}$ with $D > 1$ and n the n th Newton iteration. ρ is known as the penalty parameter in ADMM.

B

The iterative solution to Equation (A.3) requires the computation of the Jacobian $DF(x)$ and its corresponding adjoint $DF^H(x)$ operator, with the forward operator $F(x)$ denoted in Equation (4). Note that the forward operator can be split into two nonlinear operators: the parallel imaging operator ($P\mathcal{F}M\mathcal{S}$) and multi-echo signal model operator (\mathcal{B}). Since the first one has already been implemented in BART for parallel imaging as nonlinear inversion (NLINV) [28],

only the second operator is required to be implemented. Afterward, the two nonlinear operators can be chained together. Therefore, only the operator \mathcal{B} is explained in detail here.

As denoted in Equation (3), the nonlinear operator \mathcal{B} presents the mapping from the parameter maps (W, F, R_2^*, f_{B_0}) to the multi-echo images (ρ_m) , thus

$$\mathcal{B} : \mathbb{C}^{N^2 \times N_p} \mapsto \mathbb{C}^{N^2 \times E} . \quad (\text{A.6})$$

Here, N^2 denotes the image size, N_p the number of parameter maps (4 in this case) and E the number of echoes. Therefore, its Jacobian matrix $D\mathcal{B} \in \mathbb{C}^{N^2 \times E \times N_p}$. Denote \mathcal{B}_m as the operator output corresponding to the m th TE, its corresponding Jacobian is

$$\begin{aligned} D\mathcal{B}_m &= \begin{pmatrix} \frac{\partial \mathcal{B}_m}{\partial W} \\ \frac{\partial \mathcal{B}_m}{\partial F} \\ \frac{\partial \mathcal{B}_m}{\partial R_2^*} \\ \frac{\partial \mathcal{B}_m}{\partial f_{B_0}} \end{pmatrix}^T \\ &= \begin{pmatrix} e^{-R_2^* \text{TE}_m} \cdot e^{i2\pi f_{B_0} \text{TE}_m} \\ z_m \cdot e^{-R_2^* \text{TE}_m} \cdot e^{i2\pi f_{B_0} \text{TE}_m} \\ F \cdot z_m \cdot \left((-\text{TE}_m) e^{-R_2^* \text{TE}_m} \right) \cdot e^{i2\pi f_{B_0} \text{TE}_m} \\ \left(W + F \cdot z_m \right) \cdot e^{-R_2^* \text{TE}_m} \cdot (i2\pi \text{TE}_m) \cdot e^{i2\pi f_{B_0} \text{TE}_m} \end{pmatrix}^T \end{aligned}$$

The adjoint operator is then its complex conjugate transpose.

Acknowledgment

Z. T. sincerely thanks Ms. Sarina Tepan for help with the organization of patient study. Z. T. also thanks Drs. Jens Frahm and Kai Tobias Block for various discussions. Z. T. and M. U. thank DFG for the research grant TA 1473/2-1 and UE 189/4-1.

References

- [1] Caussy C, Reeder SB, Sirlin CB, Loomba R. Noninvasive, quantitative assessment of liver fat by MRI-PDFF as an endpoint in NASH trials. *Hepatology* 2018;68:763–772.
- [2] Hu HH, Branca RT, Hernando D, Karampinos DC, Machann J, McKenzie CA, et al. Magnetic resonance imaging of obesity and metabolic disorders: Summary from the 2019 ISMRM Workshop. *Magn Reson Med* 2020;83:1565–1576.
- [3] Wood JC. Impact of iron assessment by MRI. *Hematology* 2011;2011:443–450.

- [4] Hernando D, Levin YS, Sirlin CB, Reeder SB. Quantification of liver iron with MRI: State of the art and remaining challenge. *J Magn Reson Imaging* 2014;40:1003–1021.
- [5] Dixon WT. Simple proton spectroscopic imaging. *Radiology* 1984;153:189–194.
- [6] Armstrong T, Dregely I, Stemmer A, Han F, Natsuaki Y, Sung K, et al. Free-breathing liver fat quantification using a multiecho 3D stack-of-radial technique. *Magn Reson Med* 2018;79:370–382.
- [7] Zhong X, Hu HH, Armstrong T, Li X, Lee YH, Tsao TC, et al. Free-breathing volumetric liver R_2^* and proton density fat fraction quantification in pediatric patients using stack-of-radial MRI With self-gating motion compensation. *J Magn Reson Imaging* 2020;53:118–129.
- [8] Zhong X, Armstrong T, Nickel MD, Kannengiesser SAR, Pan L, Dale BM, et al. Effect of respiratory motion on free-breathing 3D stack-of-radial liver R_2^* relaxometry and improved quantification accuracy using self-gating. *Magn Reson Med* 2020;83:1964–1978.
- [9] Fessler JA, Sutton BP. Nonuniform fast Fourier transforms using min-max interpolation. *IEEE Trans Signal Process* 2003;51:560–574.
- [10] Yu H, McKenzie CA, Shimakawa A, Vu AT, Brau ACS, Beatty PJ, et al. Multiecho reconstruction for simultaneous water-fat decomposition and T_2^* estimation. *J Magn Reson Imaging* 2007;26:1153–1161.
- [11] Yu H, Shimakawa A, McKenzie CA, Brodsky E, Brittain JH, Reeder SB. Multiecho water-fat separation and simultaneous R_2^* estimation with multifrequency fat spectrum modeling. *Magn Reson Med* 2008;60:1122–1134.
- [12] Chebrolu VV, Hines CDG, Yu H, Pineda AR, Shimakawa A, McKenzie CA, et al. Independent estimation of T_2^* for water and fat for improved accuracy of fat quantification. *Magn Reson Med* 2010;63:849–857.
- [13] Reeder SB, Pineda AR, Wen Z, Shimakawa A, Yu H, Brittain JH, et al. Iterative decomposition of water and fat with echo asymmetry and least-squares estimation (IDEAL): Application with fast spin-echo imaging. *Magn Reson Med* 2005;54:636–644.
- [14] Hernando D, Kellman P, Haldar JP, Liang ZP. Robust water/fat separation in the presence of large field inhomogeneities using a graph cut algorithm. *Magn Reson Med* 2010;63:79–90.
- [15] Zhong X, Nickel MD, Kannengiesser SAR, Dale BM, Kiefer B, Bashir MR. Liver fat quantification using a multi-step adaptive fitting approach with multi-echo GRE imaging. *Magn Reson Med* 2014;72:1353–1365.

- [16] Schneider M, Benkert T, Solomon E, Nickel D, Fenchel M, Kiefer B, et al. Free-breathing fat and R_2^* quantification in the liver using a stack-of-stars multi-echo acquisition with respiratory-resolved model-based reconstruction. *Magn Reson Med* 2020;84:2592–2605.
- [17] Block KT, Uecker M, Frahm J. Model-based iterative reconstruction for radial fast spin-echo MRI. *IEEE Trans Med Imaging* 2009;28:1759–1769.
- [18] Fessler JA. Model-based image reconstruction for MRI. *IEEE Signal Processing Magazine* 2010;27:81–89.
- [19] Doneva M, Börnert P, Eggers H, Mertins A, Pauly J, Lustig M. Compressed sensing for chemical shift-based water-fat separation. *Magn Reson Med* 2010;64:1749–1759.
- [20] Wang N, Cao T, Han F, Xie Y, Zhong X, Ma S, et al. Free-breathing multitasking multi-echo MRI for whole-liver water-specific T_1 , proton density fat fraction, and R_2^* quantification. *Magn Reson Med* 2022;87:120–137.
- [21] Christodoulou AG, Shaw JL, Nguyen C, Yang Q, Xie Y, Wang N, et al. Magnetic resonance multitasking for motion-resolved quantitative cardiovascular imaging. *Nat Biomed Eng* 2018;2:215–226.
- [22] Starekova J, Zhao R, Colgan TJ, Johnson KM, Rehm JL, Wells SA, et al. Improved free-breathing liver fat and iron quantification using a 2D chemical shift-encoded MRI with flip angle modulation and motion-corrected averaging. *Eur Radiol* 2022;xx:1–12.
- [23] Buades A, Coll B, Morel JM. A non-local algorithm for image denoising. In: *Proc. IEEE Comput. Soc. Conf. Comput. Vis. Pattern Recognit.*, vol. 2; 2005. p. 60–65.
- [24] Sutton BP, Noll DC, Fessler JA. Dynamic field map estimation using a spiral-in/spiral-out acquisition. *Magn Reson Med* 2004;51:1194–1204.
- [25] Olafsson VT, Noll DC, Fessler JA. Fast joint reconstruction of dynamic R_2^* and field maps in functional MRI. *IEEE Trans Med Imaging* 2008;27:1177–1188.
- [26] Funai AK, Fessler JA, Yeo DTB, Olafsson VT, Noll DC. Regularized field map estimation in MRI. *IEEE Trans Med Imaging* 2008;27:1484–1494.
- [27] Block KT, Chandarana H, Milla S, Bruno M, Mulholland T, Fatterpekar G, et al. Towards routine clinical use of radial stack-of-stars 3D gradient-echo sequences for reducing motion sensitivity. *J Korean Soc Magn Reson Med* 2014;18:87–106.
- [28] Uecker M, Hohage T, Block KT, Frahm J. Image reconstruction by regularized nonlinear inversion – Joint estimation of coil sensitivities and image content. *Magn Reson Med* 2008;60:674–682.

- [29] Boyd S, Parikh N, Chu E, Peleato B, Eckstein J. Distributed optimization and statistical learning via the alternating direction method of multipliers. *Foundations and Trends in Machine Learning* 2010;3:1–122.
- [30] Tan Z, Voit D, Kollmeier JM, Uecker M, Frahm J. Dynamic water/fat separation and B_0 inhomogeneity mapping – Joint estimation using undersampled triple-echo multi-spoke radial FLASH. *Magn Reson Med* 2019;82:1000–1011.
- [31] Winkelmann S, Schaeffter T, Koehler T, Eggers H, Doessel O. An optimal radial profile based on the golden ratio for time-resolved MRI. *IEEE Trans Med Imaging* 2007;26:68–76.
- [32] Untenberger M, Tan Z, Voit D, Joseph AA, Roeloffs V, Merboldt KD, et al. Advances in real-time phase-contrast flow MRI using asymmetric radial gradient echoes. *Magn Reson Med* 2016;75:1901–1908.
- [33] Roemer PB, Edelstein WA, Hayes CE, Souza SP, Mueller OM. The NMR phased array. *Magn Reson Med* 1990;16:192–225.
- [34] Pruessmann KP, Weiger M, Scheidegger MB, Boesiger P. SENSE: Sensitivity encoding for fast MRI. *Magn Reson Med* 1999;42:952–962.
- [35] Griswold MA, Jakob PM, Heidemann RM, Nittka M, Jellus V, Wang J, et al. Generalized autocalibrating partially parallel acquisitions (GRAPPA). *Magn Reson Med* 2002;47:1202–1210.
- [36] Reeder SB, Bice EK, Yu H, Hernando D, Pineda A. On the performance of T_2^* correction methods for quantification of hepatic fat content. *Magn Reson Med* 2012;67:389–404.
- [37] Pruessmann KP, Weiger M, Börnert P, Boesiger P. Advances in sensitivity encoding with arbitrary k-space trajectories. *Magn Reson Med* 2001;46:638–651.
- [38] Feng L, Grimm R, Block KT, Chandarana H, Kim S, Xu J, et al. Golden-angle radial sparse parallel MRI: Combination of compressed sensing, parallel imaging, and golden-angle radial sampling for fast and flexible dynamic volumetric MRI. *Magn Reson Med* 2014;72:707–717.
- [39] Hines C, Yu H, Shimakawa A, McKenzie CA, Brittain JH, Reeder SB. T_1 independent, T_2^* corrected MRI with accurate spectral modeling for quantification of fat: Validation in a fat-water-SPIO phantom. *J Magn Reson Imaging* 2009;30:1215–1222.
- [40] Bush EC, Gifford A, Coolbaugh CL, Towse TF, Damon BM, Welch EB. Fat-water phantoms for magnetic resonance imaging validation: A flexible and scalable protocol. *J VIS EXP* 2018;139:1–9.

- [41] Uecker M, Ong F, Tamir JI, Bahri D, Virtue P, Cheng JY, et al. Berkeley Advanced Reconstruction Toolbox. In: Proceedings of the 23th Annual Meeting of ISMRM, Toronto, CAN; 2015. p. 2486.
- [42] Huang F, Vijayakumar S, Li Y, Hertel S, Duensing GR. A software channel compression technique for faster reconstruction with many channels. *Magn Reson Imaging* 2008;26:133–141.
- [43] Rosenzweig S, Holme HCM, Uecker M. Simple auto-calibrated gradient delay estimation from few spokes using Radial Intersections (RING). *Magn Reson Med* 2019;81:1898–1906.
- [44] Rosenzweig S, Scholand N, Holme HCM, Uecker M. Cardiac and Respiratory Self-Gating in Radial MRI using an Adapted Singular Spectrum Analysis (SSA-FARY). *IEEE Trans Med Imaging* 2020;39:3029–3041.
- [45] Liu CY, McKenzie CA, Yu H, Brittain JH, Reeder SB. Fat quantification with IDEAL gradient echo imaging: Correction of bias from T1 and noise. *Magn Reson Med* 2007;57:354–364.
- [46] Uecker M, Lai P, Murphy MJ, Virtue P, Elad M, Pauly JM, et al. ESPIRiT – an eigenvalue approach to autocalibrating parallel MRI: Where SENSE meets GRAPPA. *Magn Reson Med* 2014;71:990–1001.
- [47] Zhang G, Allaire D, Cagan J. Taking the guess work out of the initial guess: A solution interval method for least-squares parameter estimation in nonlinear models. *ASME J Comput Inf Sci Eng* 2021;21. 021011.
- [48] Hu Y, Wang X, Tian Q, Yang G, Daniel B, McNab J, et al. Multi-shot diffusion-weighted MRI reconstruction with magnitude-based spatial-angular locally low-rank regularization (SPA-LLR). *Magn Reson Med* 2020;83:1596–1607.
- [49] Tan Z, Hohage T, Kalentev O, Joseph AA, Wang X, Voit D, et al. An eigenvalue approach for the automatic scaling of unknowns in model-based reconstructions: Applications to real-time phase-contrast flow MRI. *NMR Biomed* 2017;30:e3835.
- [50] Breuer FA, Blaimer M, Heidemann RM, Mueller MF, Griswold MA, Jakob PM. Controlled Aliasing in Parallel Imaging Results in Higher Acceleration (CAIPIRINHA) for Multi-Slice Imaging. *Magn Reson Med* 2005;53:684–691.
- [51] Solomon E, Rigie DS, Vahle T, Paška J, Bollenbeck J, Sodickson DK, et al. Free-breathing radial imaging using a pilot-tone radiofrequency transmitter for detection of respiratory motion. *Magnetic Resonance in Medicine* 2021;85:2672–2685.

Table 4: Summary of FF values for all patients from the reference Cartesian and the proposed radial acquisition.

	Cartesian	Radial (2:47)	Radial (1:24)
Patient #1	25.07 ± 2.55	26.81 ± 3.62	25.83 ± 4.28
	19.66 ± 1.92	19.62 ± 3.73	20.47 ± 3.67
	21.28 ± 1.79	23.50 ± 2.32	24.54 ± 2.39
Patient #2	21.52 ± 2.17	21.53 ± 2.34	18.56 ± 4.02
	20.79 ± 1.81	20.56 ± 3.08	18.43 ± 4.05
	20.56 ± 1.24	23.58 ± 1.33	22.98 ± 1.69
Patient #3	13.66 ± 2.31	12.85 ± 2.79	15.36 ± 3.88
	13.64 ± 3.15	14.61 ± 3.42	16.44 ± 3.65
	14.95 ± 1.76	18.74 ± 3.52	19.89 ± 4.04
Patient #4	13.18 ± 3.55	13.12 ± 5.28	13.64 ± 5.97
	13.41 ± 3.11	13.34 ± 2.91	13.92 ± 3.52
	14.37 ± 3.04	15.17 ± 1.99	15.45 ± 2.27
Patient #5	16.77 ± 1.35	17.51 ± 0.99	13.31 ± 1.66
	19.33 ± 1.22	18.74 ± 1.29	16.86 ± 1.69
	17.34 ± 2.05	17.89 ± 1.79	17.04 ± 1.87
Patient #6	7.82 ± 2.90	5.47 ± 2.54	7.98 ± 3.73
	4.82 ± 2.03	4.87 ± 2.12	6.87 ± 2.58
	7.39 ± 1.23	6.70 ± 1.50	8.52 ± 2.45
Patient #7	9.44 ± 1.28	11.83 ± 1.85	9.34 ± 3.12
	11.24 ± 1.27	13.63 ± 1.70	13.62 ± 2.90
	12.18 ± 1.59	13.96 ± 2.26	13.36 ± 3.22
Patient #8	17.87 ± 3.10	16.71 ± 2.02	16.45 ± 3.71
	14.16 ± 1.35	14.94 ± 3.71	14.76 ± 4.01
	14.80 ± 1.40	16.42 ± 1.63	16.79 ± 2.89
Patient #9	26.60 ± 0.76	29.02 ± 1.66	28.71 ± 2.19
	26.85 ± 0.98	29.24 ± 2.21	28.95 ± 2.85
	27.45 ± 1.05	30.31 ± 1.53	30.08 ± 2.34
Patient #10	6.82 ± 1.30	8.65 ± 2.71	7.55 ± 4.20
	6.33 ± 0.92	7.25 ± 1.82	6.41 ± 3.12
	5.14 ± 1.49	6.73 ± 2.00	7.49 ± 3.14
Patient #11	12.38 ± 3.38	14.39 ± 3.14	15.34 ± 4.05
	11.97 ± 2.53	11.24 ± 4.08	12.59 ± 4.94
	12.33 ± 1.30	15.48 ± 2.23	13.83 ± 4.02
Patient #12	1.74 ± 2.39	6.81 ± 3.68	10.25 ± 5.33
	3.36 ± 3.51	6.64 ± 3.02	8.05 ± 3.87
	8.30 ± 5.51	6.23 ± 2.63	7.65 ± 3.65
Patient #13	25.62 ± 1.68	25.60 ± 2.89	28.64 ± 2.86
	28.80 ± 1.35	28.55 ± 2.19	29.15 ± 2.76
	30.55 ± 1.78	30.74 ± 1.61	31.25 ± 3.41
Patient #14	8.65 ± 2.87	11.48 ± 2.01	11.82 ± 3.09
	7.71 ± 2.44	14.59 ± 1.73	15.27 ± 2.20
	11.32 ± 1.81	15.21 ± 1.46	15.07 ± 2.06
Patient #15	1.41 ± 1.04	2.90 ± 1.53	8.23 ± 2.94
	3.32 ± 2.19	4.33 ± 1.95	6.01 ± 2.90
	3.30 ± 1.64	4.67 ± 2.04	4.96 ± 2.41

Table 5: Summary of R_2^* values for all patients from the reference Cartesian and the proposed radial acquisition.

	Cartesian	Radial (2:47)	Radial (1:24)
Patient #1	65.93 ± 9.69	64.08 ± 11.38	56.72 ± 14.78
	59.00 ± 7.67	54.56 ± 9.76	54.21 ± 13.88
	64.37 ± 8.05	61.13 ± 7.22	70.36 ± 8.63
Patient #2	56.76 ± 4.63	57.58 ± 13.52	44.44 ± 22.44
	53.43 ± 6.51	46.80 ± 4.88	48.66 ± 5.86
	48.90 ± 6.77	48.46 ± 4.23	62.61 ± 5.87
Patient #3	50.30 ± 9.98	47.42 ± 9.91	43.57 ± 14.45
	53.66 ± 11.92	51.20 ± 8.97	52.30 ± 11.97
	52.94 ± 9.15	54.81 ± 10.26	60.57 ± 11.76
Patient #4	57.52 ± 13.85	54.21 ± 13.28	59.46 ± 14.17
	48.93 ± 17.38	47.89 ± 6.67	47.05 ± 7.71
	64.83 ± 8.66	65.47 ± 5.54	60.13 ± 6.56
Patient #5	52.17 ± 6.65	49.96 ± 4.98	48.01 ± 4.81
	51.61 ± 6.70	51.22 ± 2.96	52.09 ± 3.83
	55.00 ± 6.23	49.92 ± 3.57	52.25 ± 5.25
Patient #6	32.71 ± 8.34	40.98 ± 8.37	39.14 ± 11.56
	32.20 ± 5.82	28.62 ± 3.38	27.12 ± 6.21
	34.83 ± 5.85	28.93 ± 2.94	25.97 ± 3.92
Patient #7	41.27 ± 6.39	42.79 ± 5.27	42.40 ± 10.18
	48.56 ± 4.66	52.34 ± 3.92	46.31 ± 7.66
	45.07 ± 4.13	47.59 ± 6.75	50.20 ± 7.36
Patient #8	48.50 ± 10.91	50.84 ± 6.26	51.40 ± 8.10
	50.11 ± 6.90	39.33 ± 13.85	43.56 ± 15.84
	51.94 ± 4.19	53.21 ± 5.36	50.50 ± 7.45
Patient #9	68.23 ± 3.42	67.24 ± 10.13	72.99 ± 14.40
	67.82 ± 4.67	70.57 ± 8.16	74.60 ± 10.89
	74.05 ± 4.03	81.62 ± 6.64	77.14 ± 11.25
Patient #10	49.84 ± 6.23	49.62 ± 3.38	49.21 ± 7.14
	46.05 ± 3.01	48.66 ± 2.99	50.22 ± 9.66
	45.90 ± 4.85	58.33 ± 4.70	70.90 ± 8.42
Patient #11	43.59 ± 13.09	53.36 ± 7.96	47.71 ± 12.44
	50.56 ± 6.90	46.61 ± 7.59	49.93 ± 9.97
	57.28 ± 6.31	59.93 ± 3.69	61.10 ± 6.77
Patient #12	46.69 ± 30.69	54.82 ± 11.62	53.38 ± 15.59
	55.03 ± 15.29	60.74 ± 7.26	50.06 ± 14.66
	61.89 ± 22.54	51.72 ± 8.29	46.04 ± 10.79
Patient #13	63.34 ± 9.53	75.77 ± 10.40	64.83 ± 13.06
	74.00 ± 4.67	59.35 ± 10.18	56.07 ± 19.94
	71.38 ± 9.57	68.00 ± 6.87	66.23 ± 10.89
Patient #14	39.16 ± 12.64	36.50 ± 3.20	33.93 ± 5.64
	44.40 ± 6.55	42.55 ± 3.33	47.10 ± 5.59
	48.21 ± 3.82	50.52 ± 3.96	58.19 ± 6.96
Patient #15	31.44 ± 2.53	34.66 ± 5.33	28.00 ± 6.30
	34.58 ± 7.58	33.96 ± 4.72	31.77 ± 5.86
	30.83 ± 3.96	34.52 ± 3.90	30.13 ± 6.54